ARCHIVES
of
FOUNDRY ENGINEERING

ISSN (2299-2944)
Volume 2024
Issue 1/2024

121 – 128

15/1

10.24425/afe.2024.149259

Published quarterly as the organ of the Foundry Commission of the Polish Academy of Sciences

Characterization of High Pressure Water Descaling Jets for Slabs Based on Different Shape Factors

Bowen Yang [a], Guangqiang Liu [b, *], Chengcheng Xu [c], Kun Liu [a], Peng Han [a]
[a] School of Materials and Metallurgy, University of Science and Technology Liaoning, China
[b] School of Civil Engineering, University of Science and Technology Liaoning, China
[c] Cold Rolling Mill Plant, ANGANG Steel Company Limited, China
* Corresponding author: E-mail address: lgqiang0305@sina.com

Received 11.11.2023; accepted in revised form 20.02.2023; available online 18.03.2024

Abstract

The surface temperature of steel billets during hot rolling can reach up to 1200 °C. High temperature promotes rapid oxidation of the surface of steel billets, forming a dense oxide layer similar to fish scales. If not removed in a timely manner, it will damage the surface of the steel billets and exacerbate the wear of the rolls during the descaling process. There are many methods for descaling, but high-pressure water jet has become the main method for descaling due to its excellent descaling performance, low cost, and ease of use. The tip of the descaling nozzle serves as the main component, and its structural parameters affect the final descaling effect. This research changes the shape factor of the nozzle groove curve and the diameter of the nozzle throat, and performs computational fluid dynamics (CFD) simulations on the simplified nozzle external flow field. The axial velocity at the center of the jet generates a velocity peak at 0.5-1 Dc. The peak velocity increases with the increase of shape factor and throat diameter, and the influence of shape factor on the peak velocity is greater. For a constant target distance, the length of the velocity stable section along the jet impact line increases with the increase of the shape factor. The maximum value of dynamic pressure increases, and the smaller the target distance, the greater the dynamic pressure difference. The trend of water volume is roughly the same as that of dynamic pressure.

Keywords: High pressure water, Descaling nozzle, External jet, Conical grooving

1. Introduction

Among the many methods of descaling, such as abrasive water descaling, mechanical descaling, high-pressure water descaling, pickling descaling, high-pressure water descaling has become the main means of descaling due to its low cost [1]. Descaling nozzle as the main element, the structure is mostly flat fan-shaped surface nozzle, its jet surface is thin and wide, can produce a larger impact force on the impact surface [2]. Therefore, the design and placement of the nozzles will have a direct effect on the descaling performance. Nozzle exit orifice shape, geometric profile, throat diameter and grooving method all have a large influence on key jet parameters, such as external jet shape, jet coverage and exit velocity [3-4]. In addition, the width, thickness and force of the high-pressure water jet on the slab are also important parameters in assessing the effect of descaling. Strike width and thickness (descaling width and thickness) are influenced by the parameters of the nozzle outlet structure [5-6]. The dynamic pressure and water volume distribution on the impact surface can intuitively be used to derive the magnitude of the impact force, and the velocity and pressure distribution on the

central axis of the external jet can also reflect the magnitude of the impact force side by side [7-8].

In previous studies, Gongye et al. investigated the mechanism of scale skin formation on the surface of anisotropic hot forgings of 300M steel by experiment and simulation, and analysed the state of impact force on the surface of three different shapes of hot forgings, and found that the degree of difficulty of scale skin removal was as follows: flat surface < raised surface < concave surface [9]. Wen *et al*. analysed the jet behaviour of straight conical and conical nozzles by means of orthogonal experiments, CFD numerical simulations, theoretical calculations and jet experiments, and found that the cylindrical outlet surface of the straight conical nozzle is conducive to improving the hydraulic performance of the nozzle, and the impact force on the jet impact surface of the straight conical nozzle increases with the increase in the diameter of the throat opening [10]. Rouly *et al*. used the diffusion angle, arc length and aperture ratio of the nozzle as structural variables and determined the geometries of the different structures using fourth-order Bessel curves, and performed jet experiments to find that elliptical nozzles have lower dispersion rates, uniform jet fields and suitable jet widths [11]. Huang *et al*. carried out CFD numerical simulation studies on five different nozzle shapes and found that after the jet has passed through the nozzle, the pressure distribution is always in a state when it hits the surface of the object that first produces an instantaneous peak pressure and then evolves into a more stable but smaller stagnation pressure. The peak jet impact force decreases in the order of circular, rectangular, triangular, cruciform and elliptical for the same working conditions [12]. Although many previous studies have been carried out on the variation of the structural parameters of the fan jet nozzle, little research has been carried out on the effect of the variation of the shape factor of the grooving curve and the diameter of the throat orifice, determined by different grooving methods, on the final descaling rate.

In this study, CFD numerical simulation of nozzles with different structures is carried out by varying the shape factor of the nozzle notch curve and the throat diameter to investigate the jet characteristics of the flow field outside the descaling nozzle, and to obtain the distribution of the velocity and the volume of water under dynamic pressure on the centre line of the jet of nozzles with different structures. The influence of the shape factor and throat diameter on the velocity, dynamic pressure and water volume distribution at the jet impact line is determined in order to provide theoretical support for the optimisation of the structural design of the descaling nozzle and its practical use in production.

2. Model building

2.1. Mathematical modelling

1) Governing equation

It is necessary to make the following assumptions to simulate the internal flow field medium: (1) the fluid medium is an incompressible fluid; (2) Fluid media are three-dimensional, non isothermal, and stable. Based on the above assumptions, the expressions for continuity equation, momentum equation, and energy equation are as follows.

$$\frac{\partial u}{\partial x}+\frac{\partial v}{\partial y}+\frac{\partial w}{\partial z}=0 \tag{1}$$

$$\frac{\partial(\rho uu)}{\partial x}+\frac{\partial(\rho uv)}{\partial y}+\frac{\partial(\rho uw)}{\partial z}=\frac{\partial}{\partial x}\left(\mu\frac{\partial u}{\partial x}\right)+\frac{\partial}{\partial y}\left(\mu\frac{\partial u}{\partial y}\right)+\frac{\partial}{\partial z}\left(\mu\frac{\partial u}{\partial z}\right)-\frac{\partial p}{\partial x}+S_u \tag{2}$$

$$\frac{\partial(\rho vu)}{\partial x}+\frac{\partial(\rho vv)}{\partial y}+\frac{\partial(\rho vw)}{\partial z}=\frac{\partial}{\partial x}\left(\mu\frac{\partial v}{\partial x}\right)+\frac{\partial}{\partial y}\left(\mu\frac{\partial v}{\partial y}\right)+\frac{\partial}{\partial z}\left(\mu\frac{\partial v}{\partial z}\right)-\frac{\partial p}{\partial y}+S_v \tag{3}$$

$$\frac{\partial(\rho wu)}{\partial x}+\frac{\partial(\rho wv)}{\partial y}+\frac{\partial(\rho ww)}{\partial z}=\frac{\partial}{\partial x}\left(\mu\frac{\partial w}{\partial x}\right)+\frac{\partial}{\partial y}\left(\mu\frac{\partial w}{\partial y}\right)+\frac{\partial}{\partial z}\left(\mu\frac{\partial w}{\partial z}\right)-\frac{\partial p}{\partial z}+S_w \tag{4}$$

$$\frac{\partial(\rho uT)}{\partial x}+\frac{\partial(\rho vT)}{\partial y}+\frac{\partial(\rho wT)}{\partial z}=\frac{\partial}{\partial x}\left(\frac{k}{c_p}\frac{\partial T}{\partial x}\right)+\frac{\partial}{\partial y}\left(\frac{k}{c_p}\frac{\partial T}{\partial y}\right)+\frac{\partial}{\partial z}\left(\frac{k}{c_p}\frac{\partial T}{\partial z}\right)+S_T \tag{5}$$

where ρ is the density of water, kg/m^3; u, v and w are the velocity vector components in the x, y and z directions; P is the pressure on the microelement, Pa; S_u, S_v and S_w are the generalized source terms of the momentum equation; T is the temperature of the fluid, K; k is the fluid heat transfer coefficient, W/(m·K); C_p is the specific heat capacity, J/(kg K); S_T is the internal heat source of the fluid and the part where the mechanical energy of the fluid is converted into thermal energy through viscous action.

2) Turbulence model

RNG k-ε model employs the Boussinesq vortex viscosity assumption to close the Reynolds stress term, the Reynolds comparison for turbulent diffusion in the scalar field, and the inclusion of a rotation-related term in the dissipation rate equation to better handle flow in the impinging jet's near-wall region. The turbulent kinetic energy k and dissipation rate ε transport equations for the RNG k-ε turbulence model are

$$\frac{\partial(\rho k)}{\partial t}+\frac{\partial(\rho k u_i)}{\partial x_i}=\frac{\partial}{\partial x_j}\left[\alpha_k\mu_{eff}\frac{\partial k}{\partial x_j}\right]+G_k+G_b-\rho\varepsilon-Y_M+S_k \tag{6}$$

$$\frac{\partial(\rho\varepsilon)}{\partial t}+\frac{\partial(\rho\varepsilon u_i)}{\partial x_i}=\frac{\partial}{\partial x_j}\left[\alpha_\varepsilon\mu_{eff}\frac{\partial\varepsilon}{\partial x_j}\right]+C_{1\varepsilon}\frac{\varepsilon}{k}\left(G_k+C_{3\varepsilon}G_b\right)-C^*_{2\varepsilon}\rho\frac{\varepsilon^2}{k}+S_\varepsilon \tag{7}$$

where α_k and α_ε are the turbulent Prandtl number for the k and ε equations respectively, $\alpha_\varepsilon = \alpha_k = 1.39$; μ_{eff} is the effective viscosity coefficient, $\mu_{eff} = \mu + \mu_t$; μ is the dynamic viscosity coefficient; μ_t is the turbulent viscosity coefficient, $\mu_t = \rho C_\mu k^2/\varepsilon$; C_μ is the viscosity constant; G_k is the turbulent kinetic energy due to the laminar velocity gradient; G_b is the turbulent kinetic energy due to buoyancy; Y_M is the fluctuation due to diffusion of the transition in compressible turbulence; S_k, S_ε are user defined. $C^*_{2\varepsilon} = C_{2\varepsilon} + C_\mu\rho\eta^3(1 - \eta/\eta_0)/(1 + \beta\eta^3)$, $\eta = Sk/\varepsilon$; the other constants in the RNG k-ε equation take the values $C_\mu = 0.0845$, $C_{1\varepsilon} = 1.42$, $C_{2\varepsilon} = 1.68$, $\eta_0 = 4.38$, $\beta = 0.012$.

2.2. Nozzle model

1) Research programmes

The structural position of the nozzle directly affects the outlet surface of the nozzle. The shape of the outlet surface is mainly determined using the grooving method. After analyzing the traditional U-shaped groove and V-shaped groove, it has been determined that the conical curve groove is intermediate between the two. Its shape function is as follows:

$$y = -ax^b \tag{8}$$

where y is the vertical coordinate of any point P on the conic section. x represents the abscissa of point P on the conic section. a and b are called conic function constants and only depend on shape factor.

The conic function constants are related to the shape factor as follows:

$$b = -3.7116C + 1.29524C^2 + 3.52504 \tag{9}$$

$$a = 0.57169C + 0.72136C^2 + 0.12473 \tag{10}$$

where C is the shape factor.

In addition to the possible impact of changes in the shape factor of the groove curve on the outlet surface, changes in the diameter of the nozzle throat may also have an impact. Combine the two to select nozzles with different structures, with shape factors between 0.6 and 0.9 and throat diameters between 2.1 and 2.4 mm, for orthogonal experiments. Table 1 displays the orthogonal experiment table.

Table 1.
Orthogonal experiment table of nozzle shape factor and throat diameter

D \ C	0.6	0.7	0.775	0.8	0.9
2.1	C=0.6 D=2.1	C=0.7 D=2.1	C=0.775 D=2.1	0.8 2.1	0.9 2.1
2.15	C=0.6 D=2.15	C=0.7 D=2.15	C=0.775 D=2.15	0.8 2.15	0.9 2.15
2.2	C=0.6 D=2.2	C=0.7 D=2.2	C=0.775 D=2.2	0.8 2.2	0.9 2.2
2.3	C=0.6 D=2.3	C=0.7 D=2.3	C=0.775 D=2.3	0.8 2.3	0.9 2.3
2.4	C=0.6 D=2.4	C=0.7 D=2.4	C=0.775 D=2.4	0.8 2.4	0.9 2.4

2) Models and constraints

In order to reduce computational workload and consider the possible impact of different structures on the internal flow field of nozzles, it is necessary to conduct numerical simulations of the internal flow field of nozzles with different structures. This study focuses on the 642.766.27.01 nozzle used for descaling after the furnace on the 2150 production line of a hot rolling plant. The flow field inside the nozzle was modeled and meshed using Gambit software. Fig. 1. shows the computational domain model of the flow field inside the nozzle.

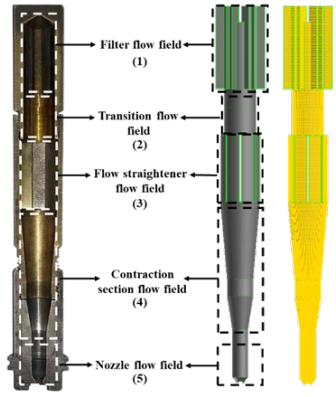

Fig. 1. Schematic diagram of the internal flow field of the descaling nozzle

In the simulation of internal flow, the fluid is water. Set the gap of the filter as the high-pressure water inlet as the pressure inlet, and the outlet of the nozzle as the pressure outlet. In the boundary condition setting, use the standard wall function to set the remaining part of the outer surface as the wall. The SIMPLE algorithm was used to achieve pressure velocity coupling, and physical weight was used to discretize the calculation domain. An implicit second order steady state solver was used for all simulations. If the energy residual is less than 10-6 and other variable residuals are less than 10-3, the calculation is considered to be converged. The relevant physical parameters and operating parameter settings are listed in Table 2.

Table 2.
Orthogonal experiment table of nozzle shape factor and throat diameter

Properties and conditions	Parameters
Inlet pressure, p_1/MPa	23
Outlet pressure, p_2/MPa	0.1
Density, ρ/(kg·m^{-3})	998.2
Specific heat capacity, C_p/(J·kg^{-1}·K^{-1})	4182
Viscosity, μ/(Pa·s)	0.001
Temperature, T/K	300

When simulating an external jet, this article takes the internal flow field below 9mm from the nozzle as the inlet of the external flow field. The fluid medium in the simplified nozzle area is water, while in areas other than the nozzle, the fluid medium is set to air. Set the simplified nozzle cross-section as the velocity inlet; The parameters of this surface are the same as those of the internal flow field, with the periphery of the nozzle set as the wall surface and the peripheral surfaces of the other calculation domains set as the pressure outlet. Fig. 2. depicts the schematic diagram of the computational domain of the external flow field.

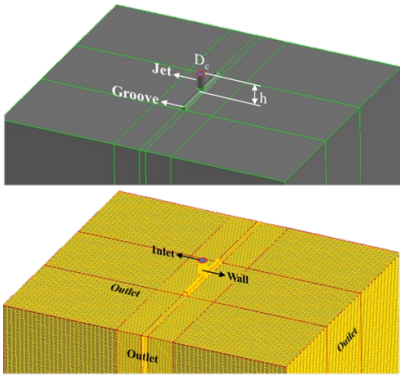

Fig. 2. Schematic diagram of the calculation domain of the external flow field of the descaling nozzle

3. Experimental setup and verification

Before conducting numerical simulations, the accuracy of the mathematical model must be verified. Therefore, based on the relevant research content, a professional experimental platform has been established. The schematic diagram of the experimental setup is shown in Fig. 3.(a), which comprises primarily of a supporting frame, background plate, nozzle, high-pressure water pump, and high-resolution camera. SolidWorks software is applied to create a simplified model of the nozzle for 3D printing. The schematic diagram of the simplified nozzle is illustrated in Fig. 4., where D is the diameter of the throat and D_O is the width of the outlet slot. Fig. 3.(b) shows the schematic diagram of the 3D printing nozzle. The high-pressure water pump is connected to the nozzle, the jet angle of the free jet of the nozzle and the jet impact width are tested at a target distance of 120 mm when the outlet pressure of the high-pressure water pump is 16 MPa (as shown in Fig. 3.(c)), and the experimental results are compared with the simulated results, as indicated by Fig. 6. The jet angles obtained from simulation and experiment are 25.9° in Fig. 5.(a) and 26.3°in Fig. 6.(b), with a relative error of 2.3%; the jet widths are respectively 68.1 mm and 65.9 mm obtained at a distance of 120mm from the nozzle outlet, with a relative error of 3.3%. The results demonstrate that the simulation results are consistent with the experimental findings.

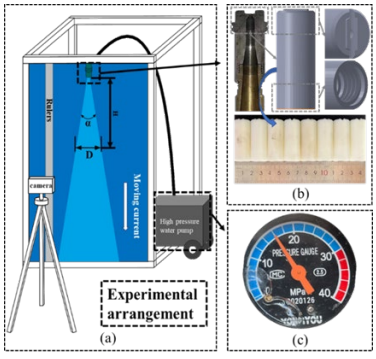

Fig. 3. Arrangement of experimental equipment (a), test nozzles (b) and pressure of experiments (c)

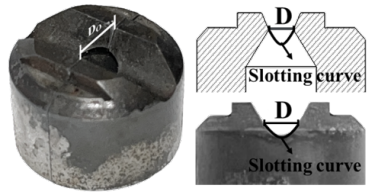

Fig. 4. Schematic diagram of high-pressure water descaling nozzle

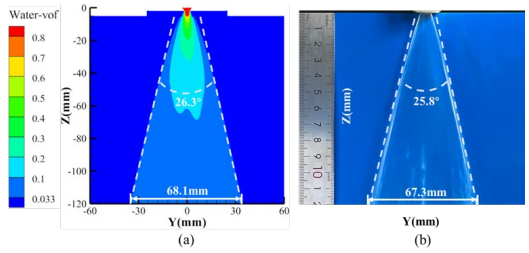

Fig. 5. Comparison of (a) simulation and (b) experimental results for external jet

4. Results and analysis

4.1. Centreline parameter distribution

By simulating the orthogonal experimental scheme mentioned above, relevant cloud maps of the external flow field were obtained. Fig. 6. illustrates the external jet velocity and dynamic pressure contours of nozzles with C=0.775 and D=2.1 at various target distances. As the target distance increases, the jet impact width and thickness gradually increase and decrease, respectively. In Fig. 6.(a), the area of the velocity core region increases as the target distance increases. The dynamic pressure is an important factor for evaluating the effective descaling area. In general, the jet impact zone with a dynamic pressure greater than 1.37 MPa is the most effective descaling zone in actual production. Fig. 6.(b) further indicates that the effective scale removal area increases with the increase of target distance. The increasing trend of width and area is similar to the expanding trend of speed core area.

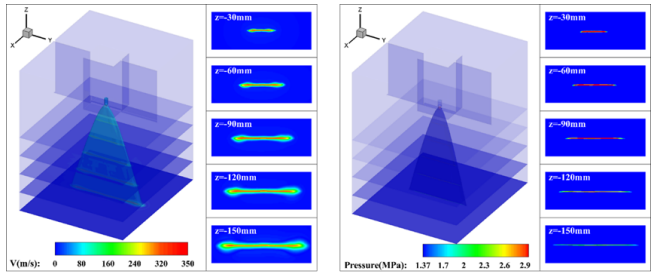

Fig. 6. Nephogram of external jet velocity (a) and dynamic pressure (b) of nozzles with C=0.775 and D=2.1 under different target distance sections

Fig. 7 shows the axial velocity distribution on the centerline of nozzle jets with different structures. It can be observed that the trend of speed change is roughly the same. The different positions of black areas with the same shape in the Fig. 7. represent different throat diameters. Analyzing the velocity distribution on the central axis of the jet, it was found that after high-pressure water was sprayed through the nozzle outlet, within a 0-1 *Dc* interval, the high-pressure jet from the narrow aperture nozzle sprayed into the free space, resulting in a rapid conversion of pressure energy and kinetic energy, causing the jet velocity at that location to surge. When the peak velocity is generated at the position of 0.5-1 *Dc*, the peak velocity increases with the increase of shape factor and throat diameter, and the influence of throat diameter is relatively small. The velocity attenuation law of external nozzle jets with different structures along the central axis is basically the same.

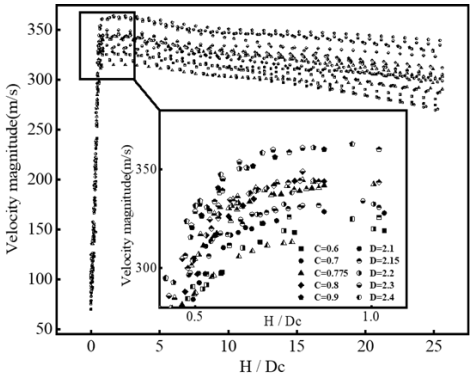

Fig. 7. Velocity distribution at the centreline of external jet nozzles with different configurations

Fig. 8. shows the axial dynamic pressure and water distribution on the centerline of the jet with different nozzle structures, and the trends of dynamic pressure and flow rate are roughly the same. In the range of 0-1 *Dc*, the rapid increase in jet velocity leads to a rapid decrease in dynamic pressure at smaller target distances. As the target distance increases, the jet from the beam gradually disperses onto the flat fan-shaped surface, and the volume of water also decreases.

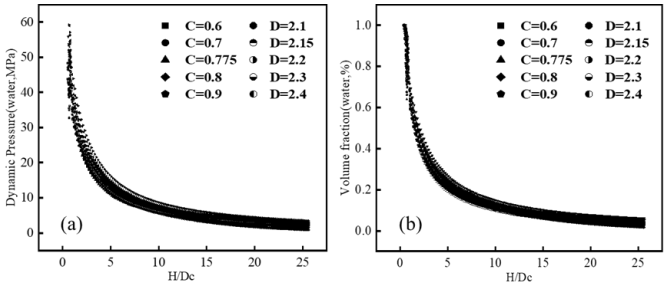

Fig. 8. Comparison of (a) simulation and (b) experimental results for external jet

4.2. Velocity radial distribution

Fig. 9. shows the velocity distribution of the external jet of the *C*=0.775, *D*=2.1 structure nozzle. It can be seen that the outermost layer on the surface of the jet is the atomization layer, which acts as the inner and outer boundary layers of the jet inward. The red area in the centre is the core of the jet. Along different target distances, in the radial direction, from the outside to the inside, the velocity increases as it gradually approaches the central axis, reaching its maximum value at the core of the jet. The law of controlling jet velocity along the axis is the same as the law analyzed in the previous section. After leaving the nozzle, the jet sprays from a smaller orifice into a larger space, causing a surge in velocity in the initial part. As the axial distance increases, the surge gradually decreases.

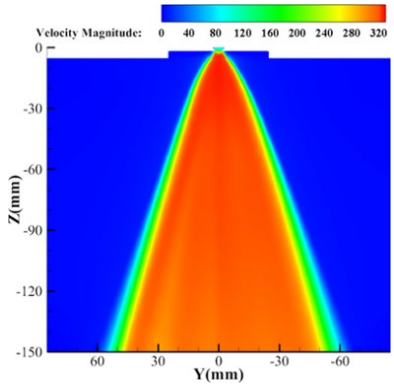

Fig. 9. Velocity distribution of the outer jet for the *C*=0.775, *D*=2.1 structure nozzle

Fig. 10. shows the radial distribution of external jet velocity under different nozzle configurations and target distances. Fig. 10. (a) shows the radial velocity distribution of nozzles with structures *C*=0.6 and *D*=2.1 at different target distances. Fig. 10. (a) shows the radial distribution of velocity at different target distances with *C*=0.6 and *D*=2.1. It can be observed that the radial velocity decays from the center to both sides. The edge side is the air velocity in the free jet basin, and the radial velocity generates a rapid increase in the atomization layer and boundary layer of the jet. A stable velocity section is formed near the velocity of 250-300m/s, which is at the core area of the jet. The stable speed segment increases with the increase of target distance.

In Fig. 10. (a), (b), (c), and (d), the shape factors increase sequentially. For the same target distance, the stable speed segment increases with the increase of shape factor. The effective width, peak radial velocity, and core area of the jet also gradually increase. In actual production use, nozzles with different shape coefficients can be selected according to different needs. Although the stable velocity section gradually increases or decreases, the peak radial velocity of the jet gradually decreases. When practical applications require more concentrated and faster impact on the surface, the target distance can be reduced. When practical applications require a smaller impact velocity but a larger jet coverage area, nozzles with larger target distances or shape coefficients can be selected.

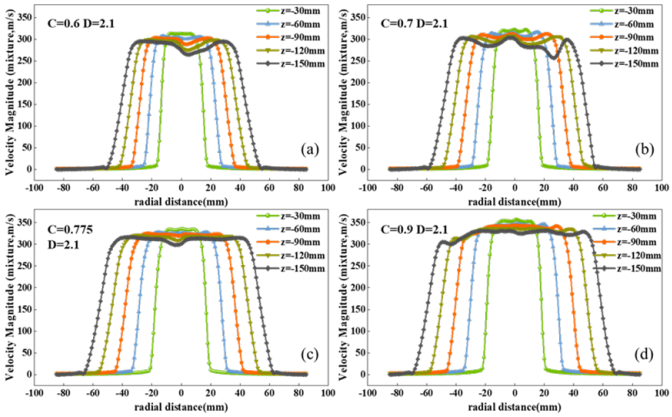

Fig. 10. Radial distribution of external jet velocity at different target distances for different nozzle configurations

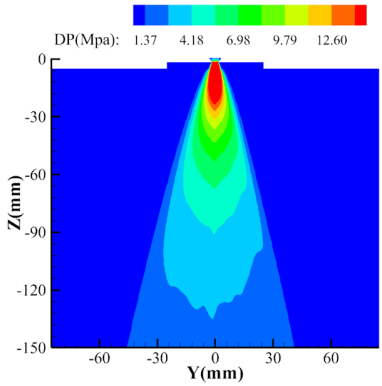

Fig. 11. Dynamic pressure distribution of the outer jet for the *C*=0.775,*D*=2.1 structure nozzle

4.3. Dynamic pressure radial distribution

The descaling effect of high-pressure water nozzles is also related to various factors, such as the process parameters, layout, and nozzle performance of the system, which can affect the descaling effect. For the external jet of the nozzle, dynamic pressure is an important physical quantity to measure the dynamic parameters of the jet. The greater the kinetic energy of the jet, the greater the impact force and the better the descaling effect. The distribution of jet dynamic pressure can comprehensively consider the distribution of jet velocity and water volume fraction, thus measuring the descaling effect. Based on actual production requirements, the equivalent surface surrounding area with dynamic pressure greater than 1.37Mpa is defined as the effective descaling area.

Fig. 11 shows the distribution of jet dynamic pressure greater than 1.37Mpa outside the nozzle with *C*=0.775 and *D*=2.1. It can be observed that the dynamic pressure distribution is different from the velocity distribution, and its effective width at the same target distance is smaller than the width of the velocity field. This is because the dynamic pressure only considers the energy generated by fluid flow, and when measuring the velocity field, it is also necessary to consider the velocity changes generated by the jet entraining the surrounding air. The effective impact surface of the jet can be intuitively obtained in the Fig. The dynamic pressure on the centerline of the jet gradually decreases with the increase of target distance. On the radial direction of the same target distance, the area with smaller dynamic pressure surrounds the dynamic pressure core area. As the radial position changes from negative to positive, the trend of dynamic pressure change also gradually increases at first, stabilizes on both sides near the centerline, and then gradually decreases.

Fig. 12. (a) shows a schematic diagram of the radial distribution of dynamic pressure at different target distances of C=0.6 and D=2.1. The radial position changes from negative to positive, and the dynamic pressure gradually increases from 0. At this time, it is the dynamic pressure of the air in the free shooting basin, which gradually increases, with peaks appearing on both sides of the center and then gradually decreasing. It is worth noting that as the target distance increases, the dynamic pressure stable region enclosed by both sides of the centerline gradually increases. At a target distance of 30mm, almost no dynamic pressure stable region can be observed, and the overall dynamic pressure distribution presents a mountain peak shape. And when the target distance is 150mm, it will be observed that the valley value on the effective impact line of the jet is lower than the actual minimum dynamic pressure required.

The shape factors in Fig. 12. (a), (b), (c), and (d) increase sequentially. Under the same target distance, the dynamic pressure stable section increases with the increase of shape factor, and the peak dynamic pressure of the external flow field of the jet increases along the impact force line, and the effective width of the jet also gradually increases. When C=0.9, the nozzle will experience significant fluctuations in the dynamic pressure stable section at target distances of 90mm, 120mm, and 150mm. Therefore, in actual production use, suitable nozzles can be selected according to needs. In this study, the nozzle shape factor and target distance gradually increased, and the effective strike width of the jet gradually increased. However, when 0.775< C <1, the effective strike width of the jet fluctuated significantly.

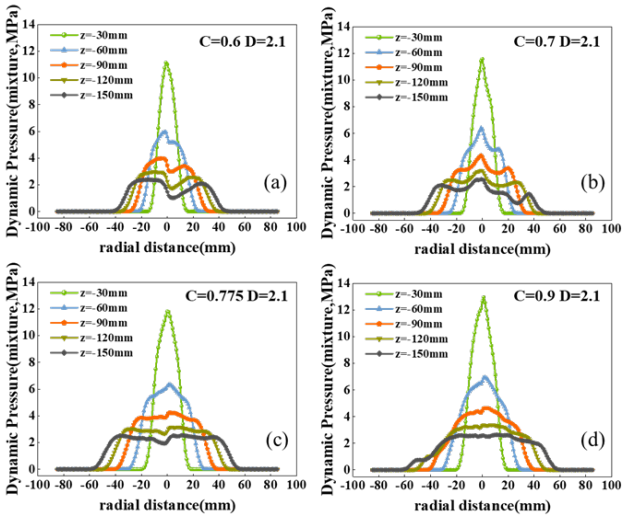

Fig. 12. Radial distribution of external jet dynamic pressure at different target distances for different nozzle configurations

4.4. Water volume radial distribution

Fig. 13. shows the distribution of volume fraction of jet water outside the nozzle with *C*=0.775 and *D*=2.1 It can be observed that the distribution of water volume fraction and velocity distribution cover an area that is roughly the same, with a higher water volume distribution at the nozzle position. As the axial distance increases, the water volume fraction gradually diverges in a fan-shaped shape, and the distribution gradually fluctuates. A larger fluctuation will affect the final descaling effect, leading to poorer results.

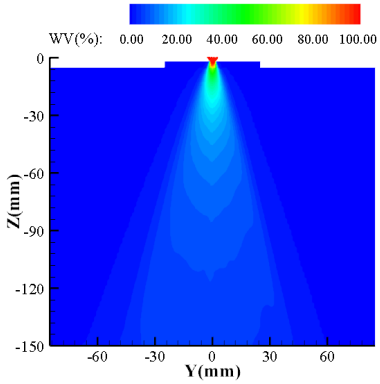

Fig. 13. Water volume fraction distribution of the outer jet for the *C*=0.775,*D*=2.1 structure nozzle

Fig. 14. (a) shows a schematic diagram of the radial distribution of dynamic pressure at different target distances of C=0.6 and D=2.1. As the radial position changes from negative to positive, the trend of water volume fraction change is similar to the radial trend of dynamic pressure. Under the same target distance, the shape factors in Figs 14 (a), (b), (c), and (d) increase sequentially, and the stable water volume fraction decreases with the increase of the shape factor. The peak water volume fraction in the external flow field of the jet decreases along the impact force action line, but the impact force action line of the jet gradually increases. Similarly to the dynamic pressure distribution, when 0.775<C<1, the impact force action line of the jet will increase, but the fluctuation is significant.

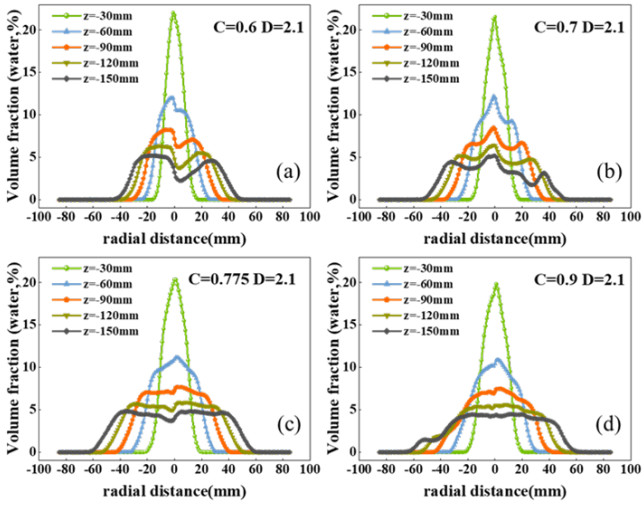

Fig. 14. Radial distribution of external jet water volume fraction at different target distances for different nozzle configurations

5. Conclusions

At the position 0.5-1 *Dc* along the centerline of the external jet velocity of the descaling nozzle, the velocity increases sharply, and the peak velocity is greatly affected by the shape factor. In the 0-1 *Dc* range, due to the rapid increase in jet velocity, the dynamic pressure decreases, the jet gradually diverges, and the water volume fraction also gradually decreases.

The radial distribution of velocity, dynamic pressure, and water volume on the action line of the impact force increases sharply when it reaches the atomization layer and boundary layer of the jet, and then reaches its peak in the core area of the jet. The velocity increases sharply along the centerline target distance and then gradually stabilizes and decreases. The dynamic pressure and water volume first decrease sharply and then tend to stabilize.

For the same shape factor, as the target distance increases, the impact force line of the jet gradually increases, and the stable length of the velocity, dynamic pressure, and water volume also increases. When the target distance is the same, the shape factor increases, and the length of the stable section for velocity, dynamic pressure, and water volume also increases. The peak dynamic pressure gradually increases, but the peak water volume gradually decreases. When 0.775 □ *C* □ 1, the effective strike width of the jet will increase, but the fluctuation is significant.

Acknowledgments

The authors are grateful for the financial support by National

Key R&D Project of China (2021YFB3702000), The Education Department Project of Liaoning Province (Study on jet behavior and interaction with melt pool of supersonic dual-Ma oxygen lance JYTMS20230932).

References

[1] Ma, F., Li, Y. & Song, Z.M. (2011). Jet performance testing of high-pressure waterjet descaling nozzles. *Advanced Materials Research*. 314, 2408-2413. https://doi.org/10.4028/www.scientific.net/AMR.314-316.2408.

[2] Baofu Kou, Pengliang Huo, Xiaohua Hou, (2020). Research on the influence of external parameters of fan-type nozzle on water jet performance. *Shock and Vibration*. 2020, 4386259, 1-16. https://doi.org/10.1155/2020/4386259.

[3] Jiang, T., Huang, Z., Li, J., Zhou, Y. & Xiong, C. (2022). Effect of nozzle geometry on the flow dynamics and resistance inside and outside the cone-straight nozzle. *ACS omega*. 7(11), 9652-9665. https://doi.org/10.1021/acsomega.1c07050.

[4] Sushma, L., Deepik, A.U., Sunnam, S.K. & Madhavi, M. (2017). CFD investigation for different nozzle jets. *Materials Today: Proceedings*. 4(8), 9087-9094. https://doi.org/10.1016/j.matpr.2017.07.263.

[5] Gu, B., Hu, R., Wang, L., & Xu, G. (2022). Study on the influence rule of high-pressure water jet nozzle parameters on the effect of hydraulic slotting. *Geofluids*. 2022, 4510194. https://doi.org/10.1155/2022/4510194.

[6] Frick, J.W. (2009). Optimisation of technologies for hydro-mechanical descaling of steel. *Metallurgical Research & Technology*. 106(2), 60-68. https://doi.org/10.1051/metal/2009015.

[7] Zhang, D., Wang, H., Liu, J., Wang, C., Ge, J., Zhu, Y., Chen, X. & Hu, B. (2022). Flow characteristics of oblique submerged impinging jet at various impinging heights. *Journal of Marine Science and Engineering*. 10(3), 399. https://doi.org/10.3390/jmse10030399.

[8] Song, X., Lyu, Z., Li, G. & Hu, X. (2017). Numerical analysis of the impact flow field of multi-orifice nozzle hydrothermal jet combined with cooling water. *International Journal of Heat and Mass Transfer*. 114, 578-589. https://doi.org/10.1016/j.ijheatmasstransfer.2017.06.106.

[9] Gongye, F., Zhou, J., Peng, J., Zhang, H., Peng, S., Li, S. & Deng, H. (2023). Study on the removal of oxide scale formed on 300 M steel special-shaped hot forging surfaces during heating at elevated temperature by a high-pressure water descaling process. *Materials*. 16, 1745, 1-14. https://doi.org/10.3390/ma16041745.

[10] Wen, J., Qi, Z., Behbahani, S. S., Pei, X. & Iseley, T. (2019). Research on the structures and hydraulic performances of the typical direct jet nozzles for water jet technology. *Journal of the Brazilian Society of Mechanical Sciences and Engineering*. 41, 1-12. https://doi.org/10.1007/s40430-019-2075-2.

[11] Rouly, E., Warkentin, A. & Bauer, R. (2015). Design and testing of low-divergence elliptical-jet nozzles. *Journal of Mechanical Science and Technology*. 29, 1993-2003. https://doi.org/10.1007/s12206-015-0420-7.

[12] Huang, F., Mi, J., Li, D. & Wang, R. (2020). Impinging performance of high-pressure water jets emitting from different nozzle orifice shapes. *Geofluids*. 2020, 8831544. https://doi.org/10.1155/2020/8831544.